A spectral boundary element algorithm for interfacial dynamics in two-dimensional Stokes flow based on Hermitian interfacial smoothing

P. Dimitrakopoulos[*], Jingtao Wang

Department of Chemical and Biomolecular Engineering, University of Maryland, College Park, MD 20742, USA

Abstract

A two-dimensional spectral boundary element algorithm for interfacial dynamics in Stokes flow is presented. The main attraction of this approach is that it exploits all the benefits of the spectral methods with the versatility of the finite element method. In addition, it is not affected by the disadvantage of the spectral methods used in volume discretization to create denser systems. To achieve continuity of the interfacial geometry and its derivatives at the edges of the spectral elements during the droplet deformation, a suitable interfacial smoothing is developed based on Hermitian-like interpolations. An adaptive mesh reconstructing procedure based on relevant lengths of the spectral elements is also described.
© 2006 Elsevier Ltd. All rights reserved.

Keywords: Boundary element method; Spectral method; Stokes flow; Interfacial dynamics

1. Introduction

The dynamics of droplets and bubbles in infinite media or in restricted geometries under viscous flows and/or gravity is a problem of great technological and fundamental interest since it is encountered in a broad range of industrial, natural and physiological processes. Industrial applications include enhanced oil recovery, coating operations, vapor condensation, waste treatment, advanced materials processing and microfluidic devices. Pharmaceutical applications include emulsions which serve as a vehicle for the transport of the medical agent to the skin. One further application constitutes the blood flow in microvessels.

Since the pioneering work of Youngren and Acrivos [1] nearly 30 years ago, interfacial dynamics in Stokes flow via the solution of boundary integral equations has developed considerably. The main benefits of this approach are the reduction of the problem dimensionality by one and the great parallel scalability. A lot of research has been done to determine and understand the deformation of droplets and bubbles in external flows, both in infinite media as well as in constrained geometries [2–4]. Considerable progress has also been made in the study of membrane-like interfaces such as those in artificial capsules and biological cells [2,5]. During the last years the interaction of deformable interfaces, e.g. suspensions of droplets, has received a lot of interest [6]. The coming years are expected to witness a growth in the application of interfacial boundary integral solutions in flows in porous media, microfluidic devices and physiological systems due to the increased interest in small scales.

During the last 30 years, several numerical methodologies have been developed for the solution of the boundary integral equations for interfacial dynamics based mainly on low-order interpolation schemes, e.g. see [2,7–10]. In the present paper we develop a high-order spectral boundary element algorithm for interfacial dynamics in Stokes flow. The main attraction of our algorithm is that it exploits all the benefits of the spectral methods (i.e. exponential convergence and numerical stability with increasing the number of discretization points) while the utilization of surface elements permits the study of the most complicated geometries [11–13]. In addition, it is not affected by the disadvantage of the spectral methods used in volume

---

*Corresponding author.

E-mail address: dimitrak@eng.umd.edu (P. Dimitrakopoulos).

discretization; namely, the requirement to deal with dense systems, because in boundary integral formulations the resulting systems are always dense, independent of the form of the discretization. Our method also exploits all the benefits of the boundary element techniques, i.e. reduction of the problem dimensionality and great parallel scalability.

We emphasize that robust spectral boundary element algorithms have been developed for the study of fixed boundary surfaces [14,15], particulate flows [16], and equilibrium interfaces under steady flows [17,18]. Therefore, with the present algorithm we seek to extend the spectral boundary element formulation to the problem of interfacial dynamic evolution.

After the mathematical formulation in Section 2, in Section 3 we present the spectral interfacial discretization. By applying a time advancing scheme, the resulting algorithm is numerically unstable due to geometric discontinuities at the edges of the spectral elements. To avoid the growth of these numerical discrepancies, in Section 4 we develop a suitable interfacial smoothing based on Hermitian-like interpolations which preserves the continuity of the interfacial geometry and its derivatives at the edges of the spectral elements during the droplet deformation. In Section 5 we present the convergence in the numerical accuracy as the number of the employed spectral points increases for the interfacial curvature and for the dynamic evolution of the interfacial shape. An adaptive mesh reconstructing procedure based on relevant lengths of the spectral elements is also described.

In the current paper we present our algorithm for two-dimensional flows. This algorithm can be employed for the study of physical problems which are by nature two-dimensional, i.e. deformation of films and (long) cylindrical fluid volumes [19,20]. It can also be employed to investigate extensively the influence of the length and width of associated three-dimensional problems (even though it cannot investigate the influence of the problem depth). The methodologies presented here can be extended in three-dimensional flows in a straightforward, though non-trivial, manner.

2. Mathematical formulation

We consider a two-dimensional droplet suspended in an infinite fluid as illustrated in Fig. 1. The droplet size is specified by its volume V or equivalently by the radius a of a circular droplet of volume $\pi a^2 = V$. The droplet (fluid 1) has density ρ_1 and viscosity $\lambda\mu$, while the surrounding fluid has density ρ_2 and viscosity μ. The gravitational acceleration is g while the surface tension γ is assumed constant. The undisturbed flow exterior to the droplet is $\boldsymbol{u}^\infty$, e.g. an extensional flow $\boldsymbol{u}^\infty = G(x, -y)$ or a simple shear flow $\boldsymbol{u}^\infty = G(y, 0)$, where G is the shear rate. In this study, the characteristic length a is used as the length scale while the time is scaled with the flow time scale G^{-1}.
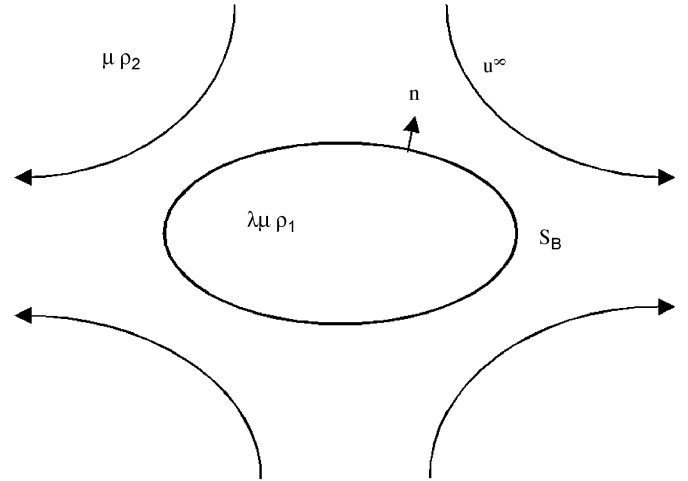

Fig. 1. Fluid droplet suspended in a surrounding fluid.

The capillary number Ca and Bond number B_d are defined by

$$Ca = \frac{\mu G a}{\gamma}, \quad B_d = \frac{(\rho_1 - \rho_2)ga^2}{\gamma}. \tag{1}$$

These dimensionless parameters represent the ratio of viscous flow forces and gravitational forces to interfacial forces, respectively.

The governing equations in fluid 2 are the Stokes equations together with continuity

$$\boldsymbol{\nabla}\cdot\boldsymbol{\sigma} = -\boldsymbol{\nabla}p + \mu\nabla^2\boldsymbol{u} = 0, \tag{2}$$

$$\boldsymbol{\nabla}\cdot\boldsymbol{u} = 0 \tag{3}$$

while in the droplet, the same equations apply with the viscosity replaced by $\lambda\mu$.

At the interface, the boundary conditions on the velocity $\boldsymbol{u}$ and surface stress $\boldsymbol{f}$ are

$$\boldsymbol{u}_1 = \boldsymbol{u}_2, \tag{4}$$

$$\Delta\boldsymbol{f} = \boldsymbol{f}_2 - \boldsymbol{f}_1 = \gamma(\boldsymbol{\nabla}\cdot\boldsymbol{n})\boldsymbol{n} + (\rho_2 - \rho_1)(\boldsymbol{g}\cdot\boldsymbol{x})\boldsymbol{n}. \tag{5}$$

Here, the subscripts designate quantities evaluated in fluids 1 and 2, respectively. The surface stress is defined as $\boldsymbol{f} = \boldsymbol{\sigma}\cdot\boldsymbol{n}$ where $\boldsymbol{n}$ is the unit normal which we choose to point into fluid 2. The pressure as defined in $\boldsymbol{\sigma}$ is the dynamic pressure; hence the gravity force is absent from Eq. (2) and appears in the interfacial stress boundary condition, Eq. (5).

The velocity at a point $\boldsymbol{x}_0$ on the droplet surface S_B may be described by the boundary integral equation

$$(1 + \lambda)\boldsymbol{u}(\boldsymbol{x}_0) - 2\boldsymbol{u}^\infty(\boldsymbol{x}_0)$$
$$= -\frac{1}{2\pi\mu}\int_{S_B}[\boldsymbol{S}\cdot\Delta\boldsymbol{f} - (1 - \lambda)\mu\boldsymbol{T}\cdot\boldsymbol{u}\cdot\boldsymbol{n}]\,\mathrm{d}S, \tag{6}$$

where S_{ij} is the fundamental solution for the two-dimensional Stokes equations and T_{ijk} the associated stress

defined by

$$S_{ij} = -\delta_{ij} \ln r + \frac{\hat{x}_i \hat{x}_j}{r^2}, \quad T_{ijk} = -4 \frac{\hat{x}_i \hat{x}_j \hat{x}_k}{r^4}, \quad (7)$$

where $\hat{x} = x - x_0$ and $r = |\hat{x}|$ [21,22]. Similar equations hold in the presence of solid boundaries and for drop suspensions [6,17].

Although the governing equations and boundary conditions are linear in u and f, the problem of determining the dynamic droplet shape constitutes a non-linear problem, i.e. the velocity u, stress f and curvature $\nabla \cdot n$ are non-linear functions of the geometrical variables describing the interface shape.

3. Numerical method

3.1. Spectral boundary discretization

The numerical solution of the boundary integral equation, Eq. (6), is achieved through an extension of the spectral boundary element method for fixed surfaces discussed in Refs. [14,15]. The initial interface is divided into a moderate number N_E of elements as shown in Fig. 2. The geometric variables on each element are discretized using Lagrangian interpolation in terms of a parametric variable ξ on the interval $[-1, 1]$, e.g.

$$x(\xi) = \sum_{i=1}^{N_B} x(\xi_i) h_i(\xi), \quad (8)$$

where h_i is the $(N_B - 1)$-order Lagrangian interpolant polynomial. The physical variables u and f are represented similarly. The base points ξ_i for the interpolation are chosen as the zeros of N_B-order orthogonal polynomials; this yields the spectral convergence associated with the orthogonal polynomial expansion. The spectral element method may employ either basis points in the interior of

the elements, i.e. Gauss-type points, or interior points along with the end points on each element, i.e. Gauss–Lobatto points.

The Gauss-type points may be derived from the Jacobi polynomials defined by

$$P_N^{(\alpha,\beta)}(\xi) = \frac{1}{2^N} \sum_{m=0}^{N} \binom{N+\alpha}{m} \binom{N+\beta}{N-m} (\xi-1)^m (\xi+1)^{N-m}, \quad (9)$$

where the constants α and β are greater than -1 [11,23]. Different values of α and β yield diverse orthogonal polynomials, e.g. $\alpha = \beta = 0$ yields the Legendre polynomials while $\alpha = \beta = -\frac{1}{2}$ produces the Chebyshev polynomials. Note that equal values of the two parameters, α and β, result in points symmetric around zero in the interval $[-1, 1]$. As the value of $\alpha = \beta$ approaches -1, the roots are closer to the ends of the interval; larger values produce roots closer to the center of the interval $[-1, 1]$ (see Fig. 3). Thus, by choosing different values of $\alpha = \beta$ we can change the distribution of the basis points. This distribution can also be controlled by employing appropriate stretching functions. Similarly to the interior Gauss Jacobi points, Gauss–Lobatto Jacobi points can also be derived which include the end points (± 1); the distribution of the interior points is again controlled by the associated parameters α and β.

The discretized expressions for the geometry and the physical variables are substituted into the boundary integral equations yielding a linear system of algebraic equations $u = Af + Bu$. The system matrices A and B are defined as integrals of the kernels S and T and the basis functions over the set of the surface elements. The numerical integration is performed by Gauss–Legendre quadrature with the aid of variable transformations as described in Ref. [14]. We emphasize that to achieve the accuracy reported in this paper, the integration error
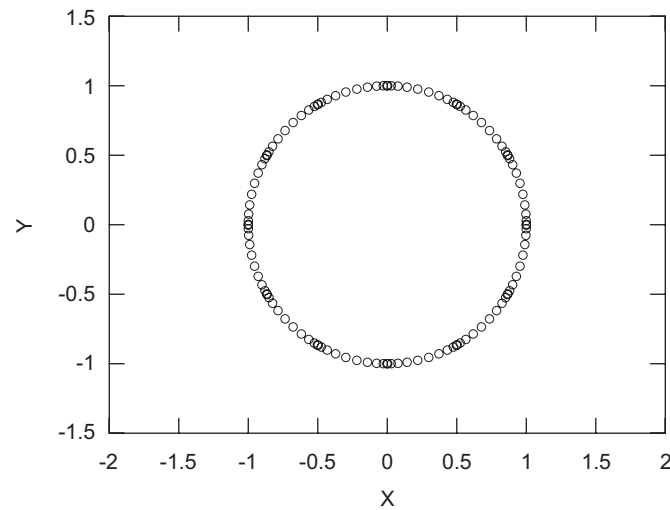

Fig. 2. Spectral boundary element discretization of a circular droplet into $N_E = 12$ equal-size elements. On each spectral element, $N_B = 10$ Gauss–Chebyshev basis points are defined.
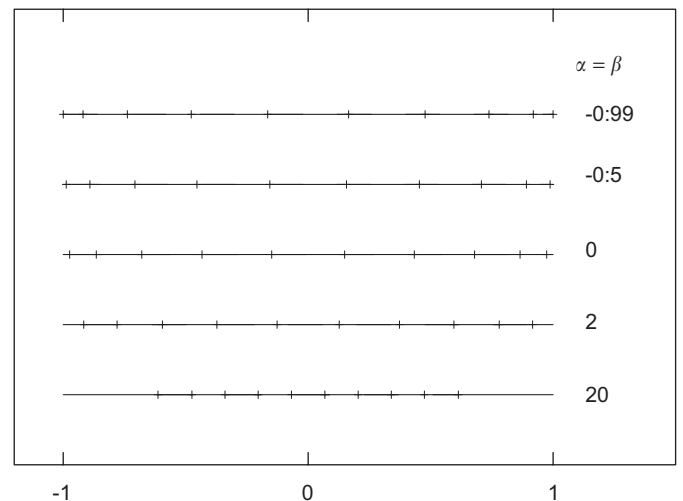

Fig. 3. The distribution in $[-1, 1]$ of $N_B = 10$ roots of Jacobi polynomials for $\alpha = \beta = -0.99, -0.5, 0, 2, 20$.

should be smaller than the error associated with the time step and the spectral interpolation.

3.2. Explicit time-integration algorithm

In order to determine the shape of the drop as a function of time, an explicit time-integration algorithm is employed to solve the kinematic condition at the interface

$$\frac{\mathrm{d}\boldsymbol{x}}{\mathrm{d}t} = (\boldsymbol{u}\cdot\boldsymbol{n})\boldsymbol{n} + U_t\boldsymbol{t}, \tag{10}$$

where the first term at the right-hand side denotes the contribution of the normal interfacial velocity while the second term denotes the contribution of some velocity tangential to the interface. (Note that $\boldsymbol{t}$ is the unit tangent vector to the interface.) The interfacial shape is dictated by the normal interfacial velocity; the tangential velocity U_t may be employed to produce a more even distribution of the spectral points as the interface deforms with time. In this study, we usually employ the tangential velocity $U_t = c_t(\boldsymbol{u}\cdot\boldsymbol{t})$ with $0.3 < c_t < 1$ far from equilibrium; close to equilibrium we set $c_t = 0$.

The time step Δt should be sufficiently small to ensure numerical stability, the well-known Courant condition which in dimensionless form may be written as

$$\Delta t < O(Ca\,\Delta x_{\min}), \tag{11}$$

where $\Delta x_{\min}$ is the minimum grid spacing [7–10]. We emphasize that the Courant condition is associated with the explicit nature of the time integration and thus it is independent of the type of the interfacial discretization. In our studies we usually employ high-order time-integration schemes (e.g. the fourth-order Runge–Kutta method) so that the numerical error associated with the time integration is small enough, i.e. at the same order as the error due to the spectral discretization.

If we apply the advancing scheme described above without any (additional) geometric constraints, the resulting algorithm is unstable as shown in Fig. 4 for a droplet under extensional flow with $Ca = 0.175$ and $\lambda = 0.5$. The numerical instability is caused by the discontinuities at the edges of the spectral elements as shown in Fig. 4(b), i.e. discontinuities of the geometry (i.e. position) and its derivatives (i.e. tangent and normal vectors, and curvature). In particular, starting from an initial smoothed interfacial shape, the geometry and its derivatives, derived by the time integration of Eq. (10) above, show discrepancies at the edges of the spectral elements. These discrepancies are caused by differences in the numerical accuracy across neighbor spectral elements and thus they are very small after one or a few time steps but may grow substantially with time if left unattended. To avoid the growth of the numerical discrepancies at the edges of the spectral elements, we smooth the interfacial geometry at the end of each time step as discussed in the next session.
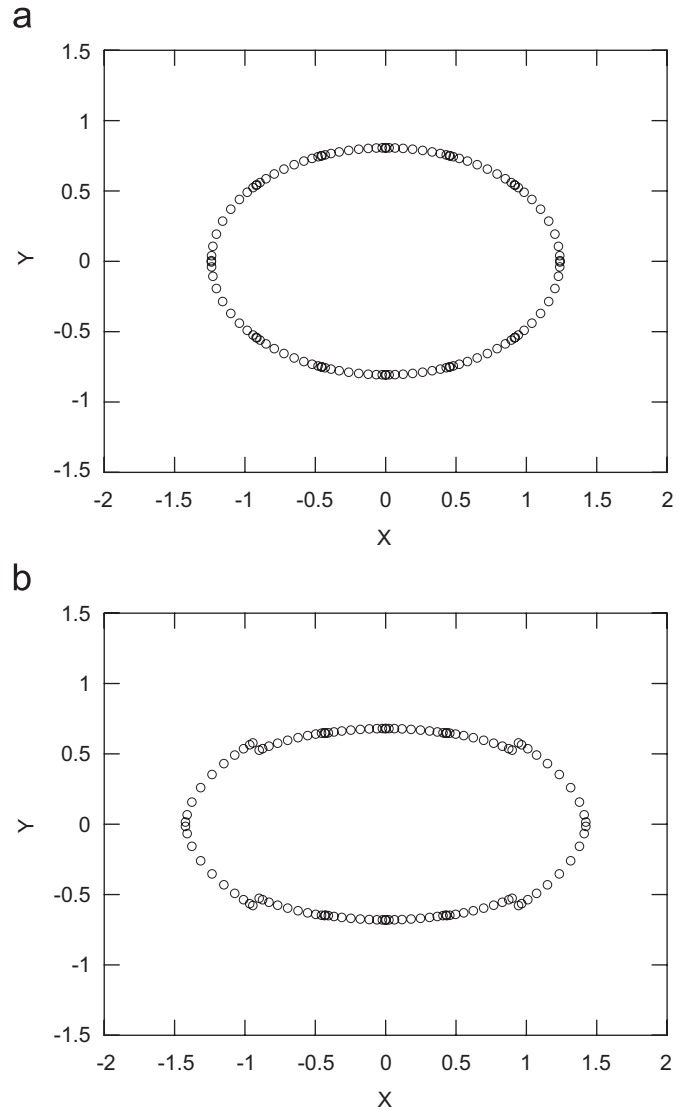

Fig. 4. Time evolution of a droplet in an extensional flow $\boldsymbol{u}^\infty = G(x, -y)$ for $Ca = 0.175$ and $\lambda = 0.5$. The initial circular interface at time $t = 0$ is divided into $N_E = 12$ equal-size spectral elements with $N_B = 10$ basis points while the fourth-order Runge–Kutta scheme is used with $\Delta t = 0.005$. No interfacial smoothing is employed. The droplet shape is shown for (a) time $t = 0.25$ (i.e. time step $N_{\text{step}} = 50$), and (b) time $t = 0.6$ or $N_{\text{step}} = 120$. The droplet initial shape is shown in Fig. 2.

4. Interfacial smoothing

4.1. First-order smoothing scheme

Our first-order smoothing scheme eliminates the discrepancy in the position, the tangent and normal vectors at the edges across neighbor spectral elements appearing during the interfacial deformation. The smoothing process involves two stages: first we smooth the geometry and its first derivatives at the element edges, and then we update the position of all points on each spectral element by employing a suitable Hermitian interpolation.

Let the non-smoothed interfacial shape at time $t + \Delta t$, derived by the time integration of Eq. (10) above, be identified as $x^{old}(\xi)$ where ξ is the parametric variable describing the interface. To perform the interfacial smoothing, we first average the position x of the edge points across neighbor elements, e.g.

$$x_a^{new} = x_b^{new} = \frac{(x_a^{old} + x_b^{old})}{2} \tag{12}$$

(where the subscripts a and b denote neighbor elements). The next step is to achieve continuity of the tangent vector $t = (dx/d\xi)/|dx/d\xi|$ at the edges of the spectral elements. To achieve this we first average the tangent vector at the edges of neighbor elements, e.g.

$$t_a^{new} = t_b^{new} = \frac{(t_a^{old} + t_b^{old})}{2}. \tag{13}$$

The new tangent vector is also normalized so that $|t^{new}| = 1$.

Both the position and the tangent vector at the edge points are now continuous across the elements. The updated derivative $(dx/d\xi)^{new}$ at the end points of each spectral element is determined by

$$\left(\frac{dx}{d\xi}\right)^{new} = \left|\frac{dx}{d\xi}\right|^{old} t^{new}. \tag{14}$$

At this point, we want to employ this updated information at the edge points to derive a smoothed interfacial shape. To achieve this goal, we employ a suitable Hermitian interpolation which utilizes function and first derivative values at the end points but only function values at the interior points developed in Ref. [24]

$$f(x) = (x^2 - 1)^2 \sum_{i=1}^{M} \frac{1}{(x_i^2 - 1)^2} \prod_{j \neq i}^{M} \left(\frac{x - x_j}{x_i - x_j}\right) f(x_i)$$

$$+ \prod_{j=1}^{M} \left(\frac{x - x_j}{-1 - x_j}\right) \frac{(x - 1)^2}{4} (x + 1) f'(-1)$$

$$+ \prod_{j=1}^{M} \left(\frac{x - x_j}{1 - x_j}\right) \frac{(x + 1)^2}{4} (x - 1) f'(+1)$$

$$+ \prod_{j=1}^{M} \left(\frac{x - x_j}{-1 - x_j}\right) \frac{(x - 1)^2}{4} [1 + b_{(-1)}(x + 1)] f(-1)$$

$$+ \prod_{j=1}^{M} \left(\frac{x - x_j}{1 - x_j}\right) \frac{(x + 1)^2}{4} [1 - b_{(+1)}(x - 1)] f(+1). \tag{15}$$

The function values $f(\pm 1)$ and the first derivatives $f'(\pm 1)$ correspond to the smoothed position x and the updated $(dx/d\xi)$ of the edge points, respectively. The coefficients $b_{(-1)}$ and $b_{(+1)}$ are chosen to yield zero slope at the

element edges,

$$b_{(-1)} = -\left[\sum_{j=1}^{M}\left(\frac{1}{x - x_j}\right) + \frac{2}{x - 1}\right]_{x = -1}$$

$$= \sum_{j=1}^{M}\left(\frac{1}{1 + x_j}\right) + 1, \tag{16}$$

$$b_{(+1)} = +\left[\sum_{j=1}^{M}\left(\frac{1}{x - x_j}\right) + \frac{2}{x + 1}\right]_{x = +1}$$

$$= \sum_{j=1}^{M}\left(\frac{1}{1 - x_j}\right) + 1. \tag{17}$$

To preserve the degrees of freedom of our spectral discretization, on each spectral element we determine $(N_B - 4)$ interior Jacobi points from the existing N_B spectral points by typical Lagrangian interpolation. We emphasize that the position and the first derivative at the two end points of each element count for the missing four degrees of freedom.

By combining these interior Jacobi points with the smoothed position x and the first-order derivatives $(dx/d\xi)$ at the edge points, the Hermitian interpolation, Eq. (15), is employed on each spectral element (with $M = N_B - 4$) to produce a new set of N_B spectral points which represents the final smoothed interfacial shape at time $t + \Delta t$.

In Fig. 5 we show the time evolution of the droplet presented earlier in Fig. 4 after we employ our first-order smoothing scheme. In contrast to Fig. 4, the drop interface is now continuous across the spectral elements at all times (e.g. well past equilibrium where we terminated our computations).
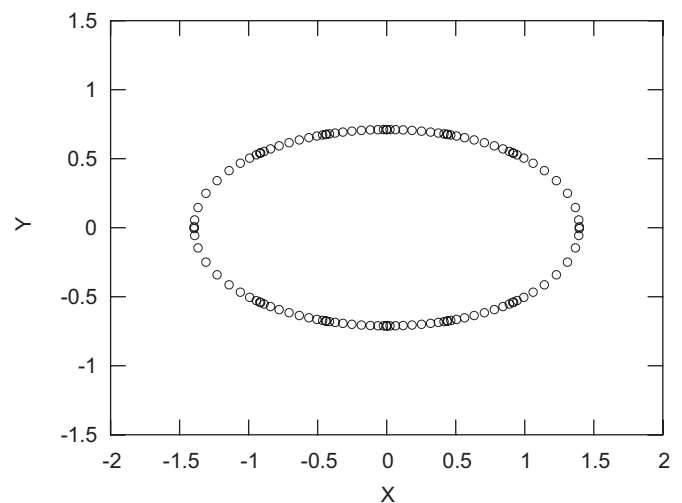

Fig. 5. Time evolution of a droplet in an extensional flow for the same parameters as in Fig. 4 except than now interfacial smoothing is employed after each time step. The droplet shape corresponds to time $t = 0.6$. The drop interface is continuous across the spectral elements at all times.

4.2. Second-order smoothing scheme

We have also developed a second-order smoothing scheme which achieves continuity of the position, tangent/normal vector and curvature at the edges of the spectral elements to account for the possibility that the curvature continuity is required explicitly. The second-order smoothing is based on a new Hermitian interpolation which employs the function values at the end points along with their first and second derivatives but only function values at the interior points, i.e.

$$
\begin{aligned}
(x) = {}& (x^2-1)^3 \sum_{i=1}^{M} \frac{1}{(x_i^2-1)^3} \prod_{j\neq i}^{M} \left(\frac{x-x_j}{x_i-x_j}\right) f(x_i) \\
& + \prod_{j=1}^{M} \left(\frac{x-x_j}{-1-x_j}\right) \frac{(x-1)^3}{-8} \frac{(x+1)^2}{2} f''(-1) \\
& + \prod_{j=1}^{M} \left(\frac{x-x_j}{1-x_j}\right) \frac{(x+1)^3}{8} \frac{(x-1)^2}{2} f''(+1) \\
& + \prod_{j=1}^{M} \left(\frac{x-x_j}{-1-x_j}\right) \frac{(x-1)^3}{-8}(x+1)[1+b_{(-1)}(x+1)] f'(-1) \\
& + \prod_{j=1}^{M} \left(\frac{x-x_j}{1-x_j}\right) \frac{(x+1)^3}{8}(x-1)[1-b_{(+1)}(x-1)] f'(+1) \\
& + \prod_{j=1}^{M} \left(\frac{x-x_j}{-1-x_j}\right) \frac{(x-1)^3}{-8}[1+b_{(-1)}(x+1) \\
& \quad + d_{(-1)}(x+1)^2] f(-1) \\
& + \prod_{j=1}^{M} \left(\frac{x-x_j}{1-x_j}\right) \frac{(x+1)^3}{8}[1-b_{(+1)}(x-1) \\
& \quad + d_{(+1)}(x-1)^2] f(+1),
\end{aligned}
\tag{18}
$$

where the coefficients $b_{(-1)}$, $b_{(+1)}$, $d_{(-1)}$ and $d_{(+1)}$ are chosen to satisfy the conditions at the end points,

$$
b_{(-1)} = \sum_{j=1}^{M} \left(\frac{1}{1+x_j}\right) + \frac{3}{2},
\tag{19}
$$

$$
b_{(+1)} = \sum_{j=1}^{M} \left(\frac{1}{1-x_j}\right) + \frac{3}{2},
\tag{20}
$$

$$
\begin{aligned}
d_{(-1)} = {}& b_{(-1)}^2 - \frac{3}{2} b_{(-1)} \\
& - \frac{1}{2} \sum_{j=1}^{M} \sum_{k=1,k\neq j}^{M} \frac{1}{(1+x_j)(1+x_k)} + \frac{3}{2},
\end{aligned}
\tag{21}
$$

$$
\begin{aligned}
d_{(+1)} = {}& b_{(+1)}^2 - \frac{3}{2} b_{(+1)} \\
& - \frac{1}{2} \sum_{j=1}^{M} \sum_{k=1,k\neq j}^{M} \frac{1}{(1-x_j)(1-x_k)} + \frac{3}{2}.
\end{aligned}
\tag{22}
$$

In particular, $b_{(-1)}$ (or $b_{(+1)}$) ensures that the coefficient of $f'(-1)$ (or $f'(+1)$) is one for the first derivative of $f(x)$ and zero for the second derivative when x equals to -1 (or $+1$). On the other hand, $d_{(-1)}$ (or $d_{(+1)}$) ensure that the terms containing $f(-1)$ (or $f(+1)$) disappear for both the first and the second derivative of $f(x)$ when x equals to -1 (or $+1$).

The procedure for the second-order smoothing is the following.

- The position, tangent vector and curvature at the edge of neighbor elements are averaged. The averaged tangent vector and curvature are used to calculate the first and second derivatives, $(\mathrm{d}x/\mathrm{d}\xi)$ and $(\mathrm{d}^2x/\mathrm{d}\xi^2)$, at the end points.
- To preserve the degrees of freedom of our spectral discretization, on each spectral element we determine $(N_B - 6)$ interior Jacobi points from the existing N_B spectral points by typical Lagrangian interpolation. We emphasize that the position, first and second derivative at the two end points of each element count for the missing six degrees of freedom.
- By combining these interior Jacobi points with the smoothed position x and the first and second derivatives, $(\mathrm{d}x/\mathrm{d}\xi)$ and $(\mathrm{d}^2x/\mathrm{d}\xi^2)$, at the edge points, the Hermitian interpolation, Eq. (18), is employed on each spectral element (with $M = N_B - 6$) to produce a new set of N_B spectral points which represents the final smoothed interfacial shape at time $t + \Delta t$.

4.3. Overview of interfacial smoothing

Starting from an initial smoothed interfacial shape, the geometry derived by the time integration of Eq. (10) above shows discrepancies at the edges of the spectral elements, i.e. discontinuities of the geometry (i.e. position) and its derivatives (i.e. tangent and normal vectors, and curvature). (We note that physical variables which depend on these geometric variables, e.g. surface stress jump, also show discontinuities at the element edges.) These discrepancies are caused by differences in the numerical accuracy across neighbor spectral elements and thus they are very small after one or a few time steps but may grow substantially with time if left unattended.

We emphasize that these geometric discontinuities at the element edges appear even when Gauss–Lobatto points are employed on the spectral elements. In this case while the geometry may be continuous at the element edges (if adjacent elements share their end points), the geometric derivatives (e.g. tangent and normal vectors, and curvature) still show discontinuity at the elements ends.

To avoid the growth of the numerical discrepancies at the edges of the spectral elements, we smooth the interfacial geometry at the end of each time step. We emphasize that if the interfacial shape is smooth at a given time, the discrepancies at the edges of the spectral elements after the time integration of Eq. (10) are very small; thus by applying our interfacial smoothing at the end of each time step the perturbation of the interfacial geometry is very small and thus it is not expected to smooth out any physical meaningful modes. For the same reason, the interfacial smoothing does not destroy the spectral accuracy discussed in Section 5.1.

We first apply our first-order smoothing scheme; thus we formally achieve continuity of the position and the tangent vector (and thus the normal vector) at the edges of the spectral elements. For many problems we have studied so far, at both subcritical and supercritical capillary numbers, our numerical results reveal that this technique usually achieves satisfactory continuity of the curvature at the element edges, i.e. continuity of the second derivative of the interfacial geometry. However, if the first-order scheme fails to produce continuous interfacial curvature at some time instant, our algorithm applies the second-order smoothing scheme.

To see how well the interfacial continuity is satisfied, after the application of the smoothing scheme at the end of each time step, we monitor the tangent vector and the curvature at the edges of neighbor elements. For example, for the interfacial shape shown in Fig. 7(b), the tangent vectors evaluated at the edges of neighbor elements show identical value to the double precision accuracy, i.e. $O(10^{-14})$ due to the first-order smoothing scheme. The interfacial curvature also shows a very small difference across neighbor elements; for $N_B = 12$ the curvature difference is $O(10^{-9})$ and thus it is much smaller than the accuracy in calculating the interfacial deformation, i.e. $O(10^{-3})$ as shown in Fig. 7(b). (Observe that the curvature shows a rather large variation along the interfacial shape.)

This conclusion may seem to contradict the experience based on low-order interpolation algorithms where to achieve continuity of the interfacial curvature, one may need to employ an interpolation which formally preserves the continuity of both first and second derivatives of the interfacial shape (e.g. spline interpolation). The difference lies on the fact that in our case, each spectral element covers a large portion of the interfacial area where the spectral interpolation produces smooth distribution of high derivatives of the interfacial geometry. In this case, by smoothing only the position and its first derivative at the element edges, we also achieve smoothing of higher derivatives of the interfacial shape.

By implementing the smoothing scheme *after* we determine the (temporary) interfacial shape at the desired time $t + \Delta t$, we have the advantage of avoiding incorporating a smoothing technique (e.g. the Hermitian interpolation) inside the spectral element algorithm for the solution of the corresponding boundary integral equation. In addition, we have the ability to re-implement the interfacial smoothing (without having to solve again a boundary integral system) if for some reason a given smoothing scheme fails. (As mentioned above, our algorithm applies the second-order smoothing scheme if the first-order scheme fails to produce continuous interfacial curvature at some time instant.)

As a closure to this section, we emphasize that the smoothing methodology we have developed is an efficient technique to preserve the continuity of the interfacial spectral geometry and its derivatives. The entire process, including the relevant Hermitian interpolation, requires a computational cost of only $O(N)$ where $N = N_E N_B$ is the total number of spectral points on the drop. Since in these interpolations we employ high-order orthogonal polynomials, the loss of accuracy from one to the other discretization is negligible. Most importantly, our smoothing methodology preserves the main characteristic of the spectral methods, i.e. the exponential convergence in the interfacial accuracy with increasing the number of spectral points N as discussed in Section 5.1 below.

5. Properties of interfacial algorithm

In this section we present the properties of our spectral boundary element algorithm at both small and large deformations under two characteristic flows, i.e. extensional and simple shear flow. The results presented below are valid for a droplet suspended in an infinite fluid with (the non-trivial) viscosity ratio $\lambda = 0.5$ and for Bond number $B_d = 0$. Note that gravitational effects may be studied easily via the interfacial condition, Eq. (5) above.

We emphasize that, in all cases under flow conditions presented in this paper, the initial shape at time $t = 0$ corresponds to a circular droplet, i.e. we consider the problem where a steady flow is introduced into the system for all times $t > 0$. Our preference is to discretize this circular shape into equal-size spectral elements. Note that a higher accuracy may be achieved if we define smaller elements in the portions of the initial interface expected to show a higher deformation under flow conditions. In this study we avoid this so that our results represent the general case where the interfacial deformation is not known (or cannot be predicted) in advance. In all cases we employ the fourth-order Runge–Kutta method. In most of the cases reported below, the same accuracy may be achieved with a lower order method, e.g. the second or third-order Runge–Kutta scheme; this depends on the employed time step and the error associated with the spectral discretization. To facilitate the reading of the paper, some information on the numerical parameters employed for the results presented below has been included in the figures' captions.

Beyond the examples discussed below, the accuracy and correctness of our algorithm was verified by comparing our results with the analytical predictions of Richardson for $\lambda = 0$ [25], and the analytical solution of Bilby and Kolbuszewski [26] for simple shear flow with $\gamma = 0$ and several viscosities ratios. In addition, our results for the steady-state shape of droplets in different flows and for several viscosity ratios were in excellent agreement with the results of our Newton method for equilibrium interfaces under flow conditions [17].

5.1. Convergence: curvature and deformation

The exponential convergence in the numerical accuracy as the number of the employed spectral points $N = N_E N_B$ increases is clearly evident at the geometric properties of a
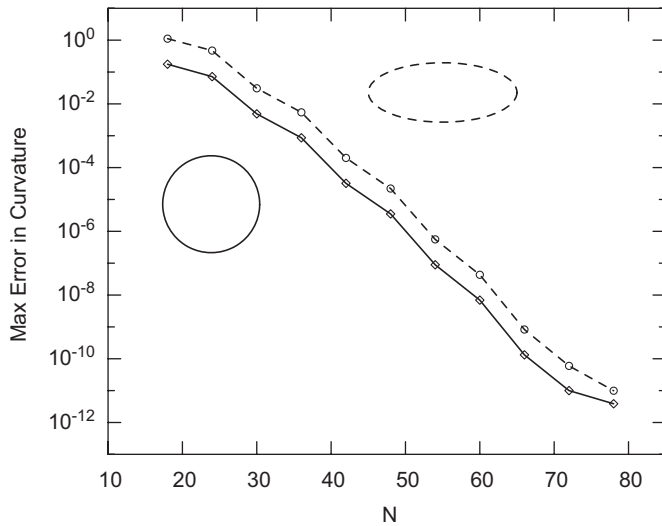
Fig. 6. The maximum absolute error in the computed curvature versus the number of spectral points $N = N_E N_B$ for a circle (—) and an ellipse with axes ratio 1:0.4 (- - - -). The exponential convergence shown in this figure was generated by employing $N_E = 6$ equal-size spectral elements and varying the number of basis points N_B from 3 to 13. The exact value was used to determine the numerical error.

given shape. Fig. 6 shows the maximum absolute error in the computed curvature as the number of spectral points N increases from 18 to 78, for a circular droplet as well as an ellipsoidal droplet with axes ratio 1:0.4. The spectral convergence is evident in the reduction of the maximum error from $\sim 10^{-1}$ for $N = 18$ to $< 10^{-11}$ for $N = 78$, i.e. a four-fold increase in the number of spectral points results in a 10^{-10} error reduction. This rapid reduction is in direct contrast to the common linear or quadratic convergence associated with low-order interpolation algorithms [7,10].

The exponential convergence in the numerical accuracy is also evident for the dynamic evolution of the interfacial shape. To determine the droplet deformation with time we monitor the droplet's longest and shortest semi-axes, L and S, respectively, as well as Taylor's deformation parameter

$$D = \frac{L - S}{L + S}. \tag{23}$$

These semi-axes are determined as the maximum and minimum distance from the droplet's centroid to the interface by employing a Newton method for the optimization problems.

Fig. 7(a) shows the convergence in the numerical accuracy of calculating the deformation parameter D for a relatively moderate deformation for a droplet with $\lambda = 0.5$ and $Ca = 0.15$ at time $t = 0.5$. Observe that by utilizing the interfacial tangential velocity $U_t = 0.5(\boldsymbol{u}\cdot\boldsymbol{t})$ the accuracy is improved by one order of magnitude. The convergence of our algorithm at large deformations is shown in Fig. 7(b) for a droplet with $\lambda = 0.5$ and $Ca = 0.25$ at time $t = 1.5$. These conditions correspond to supercritical deformation of an elongated droplet shape with ratio length over width $L/S \approx 1.95/0.477 \approx 4.09$. We note that for both capillary numbers the rapid convergence in
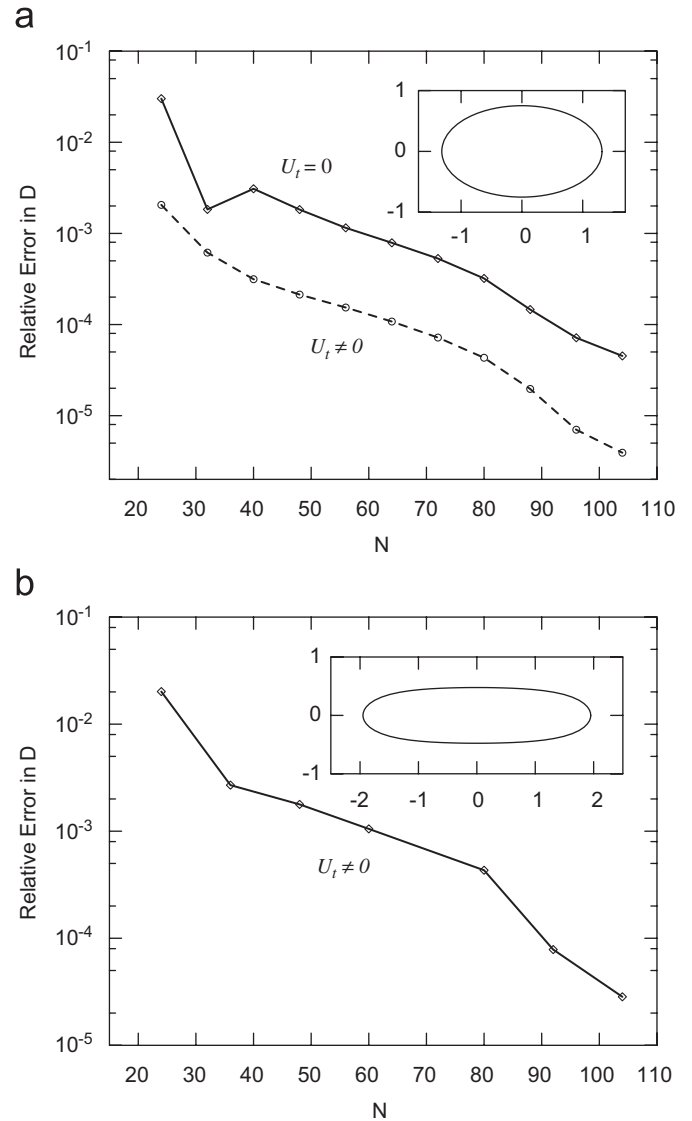

Fig. 7. Relative error in the computed drop deformation versus the total number of spectral points $N = N_E N_B$: (a) subcritical deformation for $Ca = 0.15$ and $\lambda = 0.5$ at time $t = 0.5$; (b) supercritical deformation for $Ca = 0.25$ and $\lambda = 0.5$ at time $t = 1.5$. For both capillary numbers, the curves were generated by employing $N_E = 4$ equal-size spectral elements and varying the number of basis points N_B from 6 to 26. (The results for $N_B = 28$ were used to determine the numerical error.) Also shown is the drop shape. For both Ca we employ the interfacial tangential velocity $U_t = 0.5(\boldsymbol{u}\cdot\boldsymbol{t})$ while $\Delta t = 0.001$.

the numerical accuracy as the number of spectral points increases can be approximated with a straight line in the log-linear plot, and thus our algorithm shows the expected exponential convergence due to the spectral interpolation.

5.2. Small and moderate deformations

We have performed extensive tests of our spectral algorithm by studying the dynamic evolution of droplets and bubbles in different flows and for a wide range of the parameter space, i.e. capillary number and viscosity ratio. As an example in Fig. 8 we present the time evolution
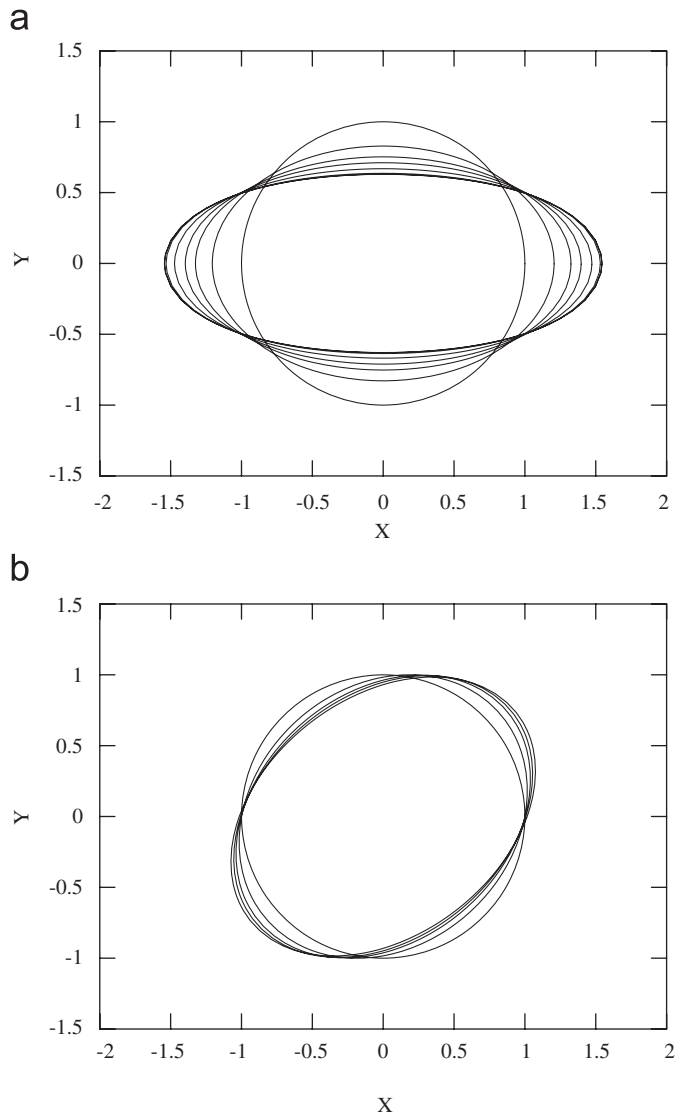
a

b

Fig. 8. Time evolution of a droplet with $\lambda = 0.5$ and $Ca = 0.175$. The interface is divided into $N_E = 12$ equal-size spectral elements with $N_B = 10$ basis points while $\Delta t = 0.005$: (a) the droplet shapes in an extensional flow at times $t = 0, 0.2, 0.4, 0.6, 1, 2, 3$; (b) the droplet shapes in a simple shear flow at times $t = 0, 0.2, 0.4, 0.6, 4$.
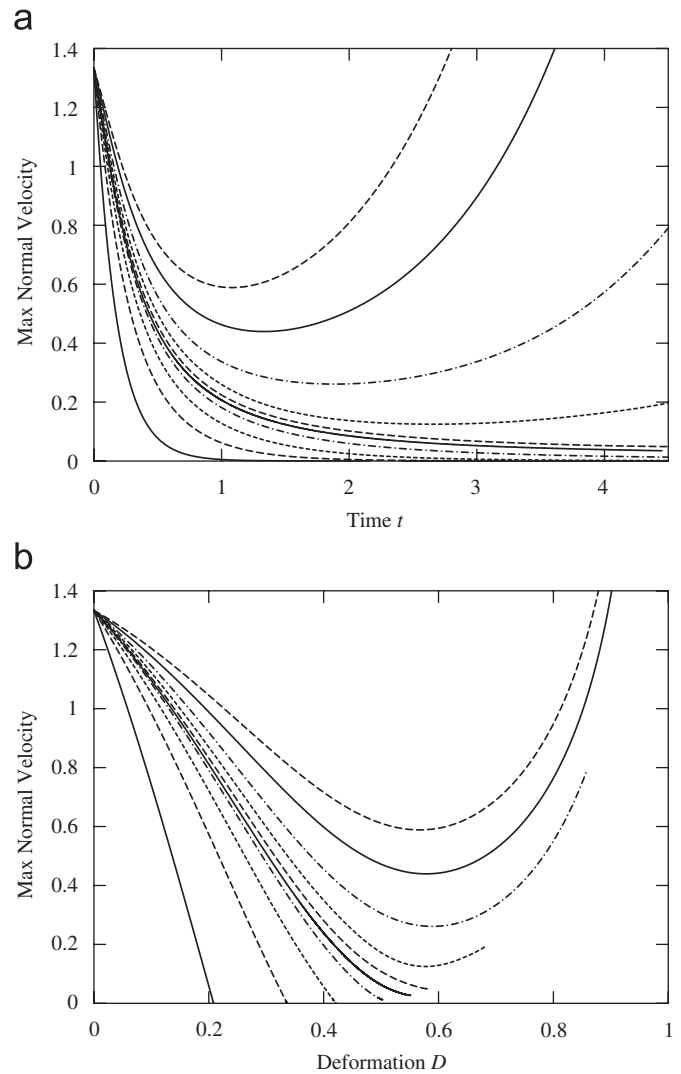
a

b

Fig. 9. Subcritical and supercritical evolution of a droplet with $\lambda = 0.5$ in an extensional flow. Capillary number: $Ca = 0.10, 0.15, 0.175, 0.19, 0.195, 0.20, 0.21, 0.225, 0.25, 0.275$: (a) maximum normal velocity versus time t; (b) maximum normal velocity versus deformation D. These curves are generated with $N_E = 12$, $N_B = 10$ and $\Delta t = 0.005$. Near the critical conditions, e.g. for $Ca = 0.195$, $t = 0.0002$ was employed.

of the interfacial shape of a droplet with $\lambda = 0.5$ and $Ca = 0.175$ in extensional and simple shear flow. These parameters correspond to subcritical conditions: as the time increases the droplet deformation increases while the interfacial normal velocity $\boldsymbol{u} \cdot \boldsymbol{n}$ diminishes until the droplet reaches equilibrium. (The evolution of D and $\boldsymbol{u} \cdot \boldsymbol{n}$ for a droplet with $Ca = 0.175$ in an extensional flow can be seen in Fig. 9.)

We have also studied the droplet evolution near the critical conditions, i.e. near the flow rate at which equilibrium interfacial shapes cease to exist. Fig. 9(a) shows the time evolution of the interfacial normal velocity of a droplet with $\lambda = 0.5$ for both subcritical and supercritical capillary numbers Ca. In the former case, the interfacial normal velocity diminishes as the droplet

reaches equilibrium; in the latter case, after an initial reduction, $\boldsymbol{u} \cdot \boldsymbol{n}$ increases as the droplet continues to elongate. Fig. 9(b) shows $\boldsymbol{u} \cdot \boldsymbol{n}$ versus deformation D. This figure reveals that the minimum normal velocity occurs at about the same value of D for the different capillary numbers Ca. The critical capillary number can also be identified as the value $Ca \approx 0.195$.

5.3. Large deformations: adaptive mesh reconstruction

For supercritical conditions, the droplet may elongate significantly; thus the original spectral discretization $\{N_E, N_B\}$ may not be sufficient to describe a very deformed interfacial shape. To resolve this issue, one may change one or both of the discretization parameters of the spectral

boundary elements, i.e. N_E and N_B. In the current implementation of our algorithm, it is more efficient to change only the number of elements. In particular, when the relevant length of a spectral element is increased above a prescribed maximum limit, the element is divided into two halves; on each one N_B basis points are defined. The opposite happens when the relevant length of a spectral element is decreased below a prescribed minimum limit; in this case the element is combined with its neighbor while N_B new basis points are defined on the resulting element. The employed time step Δt is accordingly adjusted to satisfy the Courant condition, Eq. (11).

The goal of our adaptive mesh reconstruction is to produce a reasonable spectral element discretization of the interfacial shape with respect to the element's arc length and/or the variation of curvature on it. Thus, as relevant length of a spectral element is regarded its arc length L_1 or its curvature length L_2,

$$L_1 = \int_{elem} dS, \quad L_2 = R_{\mathrm{ref}} \int_{elem} |\boldsymbol{\nabla} \cdot \boldsymbol{n}| \, dS, \qquad (24)$$

where R_{ref} is some reference radius of curvature. For problems involving surfaces in close contact, another relevant length can be considered associated with the surfaces' gap [27]. Thus our adaptive mesh procedure is similar to the ones employed in low-order algorithms, e.g. [27,28]. A difference is that our procedure is based on the size of the spectral elements, and not of successive grid points; thus it requires a smaller number of comparisons and decision making operations (i.e. divide, unite or no change).

We note that in the current implementation, when two successive elements merge, the common end point corresponds to the parametric variable $\xi = 0$ on the resulting element. This produces a reasonable distribution of the spectral points on the new element when the arc length or curvature length of the two elements does not differ substantially; our numerical tests also show that this merging works very well even in the opposite case. (Moreover, merging based on the elements' arc length or curvature length can easily be implemented, if needed.)

This strategy has been employed to determine large deformations of droplets in supercritical conditions in extensional flow. Fig. 10 shows the time evolution of the interfacial shape for $\lambda = 0.5$ and $Ca = 0.25$. Note that the initial circular shape is discretized into $N_E = 6$ equal-size spectral elements while as the drop deformation increases more elements are employed. At time $t = 4.5$ a long neck has been created as shown in Fig. 10(b); the ratio of length over the droplet width is now $L/S \approx 10.08/1.85 \approx 5.4$ and $N_E = 12$ spectral elements are employed. At time $t = 5.9$ the neck has become a very thin thread and $N_E = 28$ spectral elements are used as shown in Fig. 10(c).

Fig. 11(a) shows the relaxation of the droplet shape following a strong extensional flow. As the droplet deformation decreases towards the equilibrium circular shape, the number of spectral elements employed is also
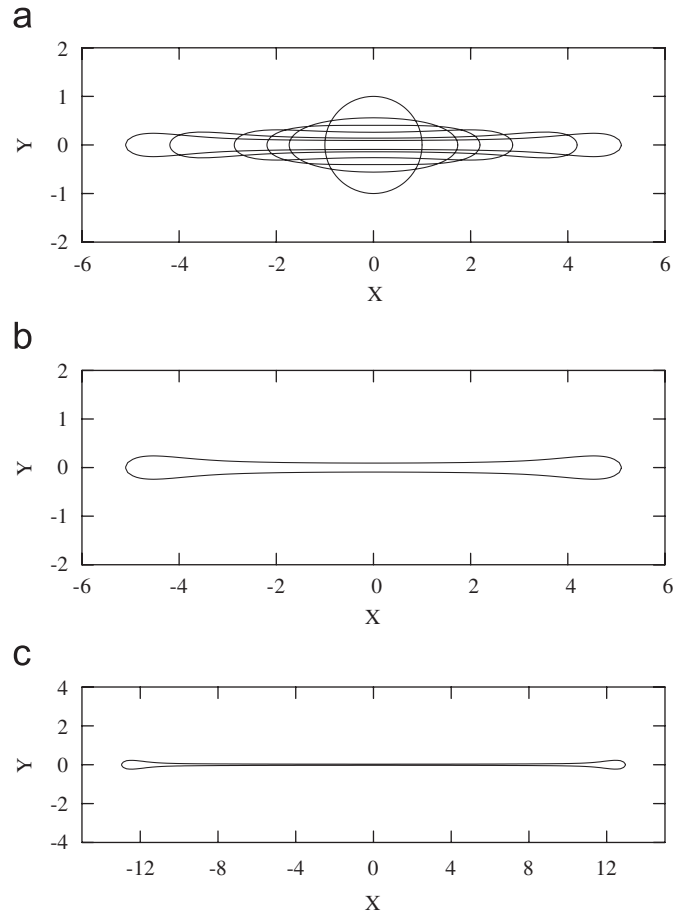

Fig. 10. Time evolution of a droplet with $\lambda = 0.5$ and $Ca = 0.25$. The original circular shape is divided into $N_E = 6$ spectral elements with $N_B = 10$ based points while the initial time step is $\Delta t = 0.005$. As the droplet deformation increases, the number of spectral elements employed is increased: (a) the droplet shape at times $t = 0, 1, 2, 3, 4, 4.5$; (b) the droplet shape at time $t = 4.5$ with $N_E = 12$; (c) the droplet shape at time $t = 5.9$ with $N_E = 28$.

decreased. The relaxation of the droplet follows a different dynamic evolution compared to the associated drop extension as the dynamic evolution of the length L and width S of the droplet reveal in Fig. 11(b). Our two-dimensional results are in qualitative agreement with the experimental findings of Ha and Leal [29], which shows that our methodology may be employed to investigate extensively the influence of the length and width of associated three-dimensional problems.

6. Conclusions

In this paper we have described a spectral boundary integral approach for interfacial dynamics in Stokes flow. To preserve the continuity of the interfacial geometry and its derivatives at the edges of the spectral elements during the droplet deformation, a suitable interfacial smoothing based on Hermitian-like interpolations was developed. Our smoothing methodology preserves the main characteristic of the spectral methods, i.e. the exponential convergence in
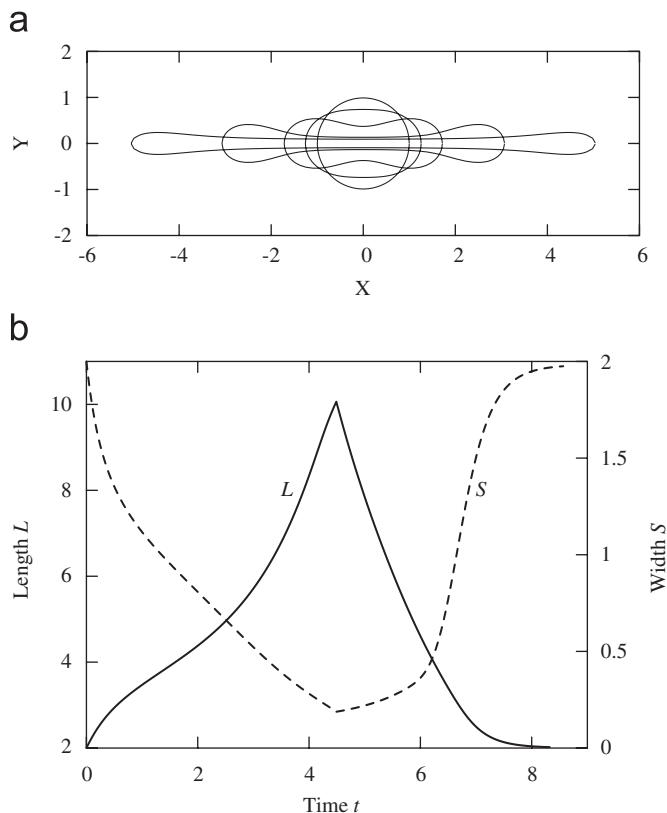
a

b

Fig. 11. Relaxation of a droplet with $\lambda = 0.5$ following an extensional flow with $Ca = 0.25$. The flow ceases at time $t = 4.5$ (the corresponding droplet shape is shown in Fig. 10(b)): (a) the droplet shapes shown correspond to times $t = 4.5, 5.5, 6.5, 7, 8.5$; (b) the time evolution of the droplet's length L and width S for the entire experiment.

the interfacial accuracy as the number of spectral points increases. An adaptive mesh reconstructing procedure based on relevant lengths of the spectral elements has also been described and its applicability to very thin interfacial necks has been demonstrated. Therefore, the current methodology can be employed for a wide range of interfacial problems in porous media, microfluidic devices and physiological systems.

Acknowledgments

References

[1] Youngren GK, Acrivos A. On the shape of a gas bubble in a viscous extensional flow. J Fluid Mech 1976;76:433–42.

[2] Pozrikidis C. Interfacial Dynamics for Stokes Flow. J Comput Phys 2001;169:250–301.

[3] Rallison JM. The deformation of small viscous drops and bubbles in shear flows. Ann Rev Fluid Mech 1984;16:45–66.

[4] Stone HA. Dynamics of drop deformation and breakup in viscous fluids. Ann Rev Fluid Mech 1994;26:65–102.

[5] Pozrikidis C, editor. Modeling and simulation of capsules and biological cells, London: Chapman & Hall; 2003.

[6] Zinchenko AZ, Davis RH. Shear flow of highly concentrated emulsions of deformable drops by numerical simulations. J Fluid Mech 2002;455:21–62.

[7] Bazhlekov IB, Anderson PD, Meijer HEH. Nonsingular boundary integral method for deformable drops in viscous flows. Phys Fluid 2004;16:1064–81.

[8] Loewenberg M, Hinch EJ. Numerical simulation of a concentrated emulsion in shear flow. J Fluid Mech 1996;321:395–419.

[9] Rallison JM. A numerical study of the deformation and burst of a viscous drop in general shear flows. J Fluid Mech 1981;109:465–82.

[10] Zinchenko AZ, Rother MA, Davis RH. A novel boundary-integral algorithm for viscous interaction of deformable drops. Phys Fluids 1997;9:1493–511.

[11] Canuto C, Hussaini MY, Quarteroni A, Zang TA. Spectral methods in fluid dynamics. Berlin: Springer; 1998.

[12] Hussaini MY, Zang TA. Spectral methods in fluid dynamics. Ann Rev Fluid Mech 1987;19:339–67.

[13] Maday Y, Patera AT. Spectral element methods for the incompressible Navier-Stokes Equations. In: Noor AK, Oden JT, editors. State of the art surveys in computational mechanics. New York: ASME; 1989.

[14] Muldowney GP, Higdon JJL. A spectral boundary element approach to three-dimensional Stokes flow. J Fluid Mech 1995;298:167–92.

[15] Occhialini JM, Muldowney GP, Higdon JJL. Boundary Integral/Spectral Element Approaches to the Navier-Stokes Equations. Int J Numer Methods Fluid 1992;15:1361–81.

[16] Pozrikidis C. A spectral-element method for particulate Stokes flow. J Comput Phys 1999;156:360–81.

[17] Dimitrakopoulos P, Higdon JJL. Displacement of fluid droplets from solid surfaces in Low-Reynolds-number shear flows. J Fluid Mech 1997;336:351–78.

[18] Dimitrakopoulos P, Higdon JJL. On the displacement of three-dimensional fluid droplets from solid surfaces in low-Reynolds-number shear flows. J Fluid Mech 1998;377:189–222.

[19] Mason G. An experimental determination of the stable length of cylindrical liquid bubbles. J Colloid Interface Sci 1970;32:172–6.

[20] Veretennikov I, Indeikina A, Chang HC. Front dynamics and fingering of a driven contact line. J Fluid Mech 1998;373:81–110.

[21] Higdon JJL. Stokes flow in arbitrary two-dimensional domains: shear flow over ridges and cavities. J Fluid Mech 1985;159:195–226.

[22] Pozrikidis C. Boundary integral and singularity methods for linearized viscous flow. Cambridge: Cambridge University Press; 1992.

[23] Abramowitz M, Stegun IA, editors. Handbook of mathematical functions with formulas, graphs, and mathematical tables. New York: Dover; 1972.

[24] Dimitrakopoulos P. Computational studies of droplet displacement in stokes flow. MS thesis, University of Illinois, 1996.

[25] Richardson S. Two-dimensional bubbles in slow viscous flows. J Fluid Mech 1968;33:475–93.

[26] Bilby BA, Kolbuszewski ML. The finite deformation of an inhomogeneity in two-dimensional slow viscous incompressible flow. Proc R Soc Lond A 1977;355:335–53.

[27] Cristini V, Blawzdziewicz J, Loewenberg M. An adaptive mesh algorithm for evolving surfaces: simulations of drop breakup and coalescence. J Comput Phys 2001;168:445–63.

[28] Kwak S, Pozrikidis C. Adaptive triangulation of evolving, closed, or open surfaces by the advancing-front method. J Comput Phys 1998;145:61–88.

[29] Ha JW, Leal LG. An experimental study of drop deformation and breakup in extensional flow at high capillary number. Phys Fluid 2001;13:1568–76.